


## Article

# Research on the Corrosion Resistance of Reactive Powder Concrete with Straw Fibers under Chloride Environment

An Wang <sup>1</sup>, Weixiang Sun <sup>2</sup>, Miao Lu <sup>2</sup>, Xi Peng <sup>3,4,\*</sup> , Hui Wang <sup>1,\*</sup> and Yao Ji <sup>1</sup>

<sup>1</sup> School of Civil Engineering and Geographic Environment, Ningbo University, Ningbo 315000, China

<sup>2</sup> China Construction Infrastructure Co., Ltd., Beijing 100020, China

<sup>3</sup> School of Civil Transportation Engineering, Ningbo University of Technology, Ningbo 315211, China

<sup>4</sup> Ningbo Roaby Technology Industrial Group Co., Ltd., Ningbo 315800, China

\* Correspondence: pengxi@nbut.edu.cn (X.P.); huiwang123@aliyun.com (H.W.)

**Abstract:** Reactive powder concrete (RPC) is widely used in large-scale bridges, and its durability in coastal areas has become a significant concern. Straw fibers have been evidenced to improve the mechanical properties of concrete, while research on their influence on the chloride corrosion resistance of RPC is deficient. Therefore, it is essential to establish the relationships between the quantities and parameters of straw fibers and the properties of the resulting concrete. In this study, the mass loss rates (MLRs), the relative dynamic modulus of elasticity (RDME), the electrical resistance (R), the AC impedance spectrum (ACIS), and the corrosion rates of steel-bar-reinforced RPC mixed with 0%–4% straw fibers by volume of RPC were investigated. A scanning electron microscope (SEM) and X-ray diffraction (XRD) were used to analyze the corrosion of steel bars. The reinforced RPC specimens were exposed to a 3% NaCl dry-wet alternations (D-As) and 3% NaCl freeze-thaw cycles (F-Cs) environment. The results show that, after adding 1%–4% straw fibers, the setting time and slump flow of fresh RPC were reduced by up to 16.92% and 12.89%. The MLRs were −0.44%–0.43% and −0.38%–0.42%, respectively, during the D-As and F-Cs. The relationship between the RDME and the fiber volume ratio was the quadratic function, and it was improved by 9.34%–13.94% and 3.01%–5.26% after 10 D-As and 100 F-Cs, respectively. Incorporating 4% straw fibers reduced the R values of the reinforced RPC specimens by up to 22.90% and decreased the corrosion rates after 10 D-As and 100 F-Cs by 26.08% and 82.29%, respectively. The impedance value was also increased. Moreover, a dense, ultra-fine iron layer and  $\alpha$ -FeO(OH) were observed in the rust of rebars by SEM and XRD, as the corrosion resistance of rebars was enhanced. The results indicate that straw fibers improved the corrosion resistance of RPC, which can serve as a protective material to inhibit concrete cracking and thereby prevent rebar oxidation. This study provides theoretical support for the investigation of surface phenomena in reinforced RPC with straw fibers.

**Keywords:** reinforced reactive powder concrete; straw fibers; chloride environment; dry-wet alternation; freeze-thaw cycle; electrochemical test; corrosion resistance



**Citation:** Wang, A.; Sun, W.; Lu, M.; Peng, X.; Wang, H.; Ji, Y. Research on the Corrosion Resistance of Reactive Powder Concrete with Straw Fibers under Chloride Environment.

*Coatings* **2024**, *14*, 961. <https://doi.org/10.3390/coatings14080961>

Academic Editor: Paolo Castaldo

Received: 11 July 2024

Revised: 26 July 2024

Accepted: 28 July 2024

Published: 1 August 2024



**Copyright:** © 2024 by the authors. Licensee MDPI, Basel, Switzerland. This article is an open access article distributed under the terms and conditions of the Creative Commons Attribution (CC BY) license (<https://creativecommons.org/licenses/by/4.0/>).

## 1. Introduction

Reactive powder concrete (RPC) is a material with excellent properties, including ultra-high strength, high impact toughness, and good volume stability [1,2]. Its performance is further enhanced by the configuration of steel bars [3–5]. The bond strength between RPC and rebars is increased by 28% compared to ordinary concrete [6]. The flexural strength of RPC increases with the number of steel bars, up to 30%, which makes it appropriate for engineering structures [7]. The utilization of RPC in reinforced concrete enables the reduction in sectional size and self-weight of the structures [8], which has great potential for application in the field of bridge engineering [9]. However, the corrosion of steel bars in coastal areas is a crucial factor affecting the service life of reinforced concrete structures [10]. When chloride ions in seawater penetrate the cracks in concrete, they

adhere to the surface of the rebar's rod passivation film and destroy it [11]. This reduces the resistivity between the negative and positive poles of the rebar and accelerates the electrochemical corrosion [12]. The volumetric expansion of chloride corrosion products gives rise to internal stresses, which result in further cracking of the concrete [13]. As chloride corrosion weakens the bond strength between steel bars and concrete, the core strength of structures is significantly degraded [14,15]. The high compactness of RPC can provide some protection for rebars; however, when cracks occur on the concrete surface, the steel bars are inevitably exposed to risk of deterioration [16]. It is an urgent problem to find new materials to prevent reinforced concrete corrosion.

Fiber materials are widely employed to improve the properties of concrete [17]. A high number of short steel fibers can improve the stress redistribution of concrete, which is advantageous for achieving excellent self-healing properties [18]. The permeability and carbonization resistance of concrete are improved by 39.1% and 31.8% by incorporating carbon nanofibers at a volume fraction of 0.3% [19]. The post-crack corrosion rate is reduced by 25% by adding 1.5% by volume of polyethylene fibers to reinforced concrete [20]. The combination of basalt fibers and polypropylene fibers produces a crack-bridging effect that enhances the chloride resistance and, consequently, the durability of concrete [21]. However, the high price of these fibers makes them impractical for large-scale engineering applications [22,23].

Straw fibers are non-corrosive plant materials, cheap and readily available [24–27]. Their good water absorption helps to reduce the initial setting time of fresh concrete, making it possible to quickly repair damaged structures [28]. Straw fibers have tiny barbs that can enhance the friction with concrete on the contact surface [29]. The compressive strength of RPC is increased by 30.5% after mixing in 3% straw fibers [30]. The inhibition of cracking by straw fibers improves the tensile and flexural properties of concrete by 17.1% and 25.8%, respectively [31]. The tight clusters between straw fibers and concrete improve the load transfer across cracks, which contributes to enhancing the compressive strength of concrete [32,33]. However, little research has focused on the corrosion resistance of RPC reinforced with straw fibers under chloride environments. In addition, excessive straw fibers may have negative effects on the properties of concrete [34]. High numbers of straw fibers will absorb water, causing the cement to dry out and shrink, which increases the risk of breaking [35]. When the length is too long, they tend to clump together and weaken the local performance of the concrete [36]. Therefore, it is vital to investigate the relationship between the quantity of straw fibers and the durability of reinforced RPC.

In this study, the corrosion resistance of RPC reinforced with straw fibers in chloride environments was investigated. The setting time and slump flow of fresh RPC were measured to study its construction feasibility. The internal defective situation of RPC was detected by ultrasonic and electrical techniques. The corrosion products of the steel bars were analyzed by Apero-2 scanning electron microscope (ThermoFisher Company, Regensburg, Germany) and Ultima-IV X-ray diffractometer (Rigaku Corporation, Tokyo, Japan). This study was to determine the optimal straw fiber content for RPC's durability, and it is anticipated that straw fibers can be used as a novel coating material to extend the working life of marine concrete structures in the future.

## 2. Experimental Procedure

### 2.1. Materials and Specimen Preparations

The common silicate cement P.O42.5 (Hangzhou Shanxin cement component Co., Ltd., Hangzhou, China) was used to produce RPC specimens. The initial and final setting times of the silicate cement were 120 min and 350 min, respectively, while the specific surface area was 350 m<sup>2</sup>/kg. The straw fibers, with a density of 35 kg/m<sup>3</sup> and an average length of 3 cm, were bought from Jiangsu Fangyuan Tong Biotechnology Co., Ltd., Xuzhou, China. The aggregate consisted of silica sand with particle sizes of 1–0.71 mm, 0.59–0.35 mm, and 0.15–0.297 mm in a mass ratio of 1:1.5:0.8. The mixture included polycarboxylic acid-based water reducer (capable of up to 40% reduction), silica fume, early-strength admixture,

and defoamer (polyether surfactant DF-04). Table 1 shows the chemical composition of raw materials.

**Table 1.** Chemical composition of raw materials (%).

Types	Chemical Composition (%)								
	SiO <sub>2</sub>	Al <sub>2</sub> O <sub>3</sub>	Fe <sub>2</sub> O <sub>3</sub>	MgO	CaO	SO <sub>3</sub>	R <sub>2</sub> O	P <sub>2</sub> O <sub>5</sub>	Loss
OPC	20.97	5.92	3.61	1.77	61.98	2.71	0.47	0	2.59
Silica Fume	90	0.8	0.6	0.8	0.4	0	7.4	0	-

Five groups of samples were prepared by adding straw fibers at 0%, 1%, 2%, 3%, and 4% by volume ratio of RPC, each comprising six specimens. A 3% NaCl solution was employed to simulate the erosion of seawater in this study [37]. Three specimens from each group were affected by dry-wet alternations (D-As), and the other three specimens were affected by freeze-thaw cycles (F-Cs). Table 2 shows the mix ratios of RPC with straw fibers. The specimens were prepared according to the GB/T 50081-2019 standard [38]. All raw materials were mixed for 480 s by the UJZ-15 mortar mixer before being poured into the mold to manufacture RPC specimens measuring 50 mm × 50 mm × 50 mm. After compacting the concrete by vibration, an 8 mm steel bar was inserted in the center of the mold shaft, and a 304 stainless steel wire mesh was placed in each specimen with a distance of 20 mm between the mesh and the position of the steel bar shaft. The molds were disassembled after 28 days of curing in a standard curing environment (with a temperature of 20 °C ± 2 °C and humidity higher than 95%) according to the GB/T50204-2015 standard [39]. After the maintenance was completed, all sets of specimens were subjected to 3% NaCl solutions for 4 days before applying D-As and F-Cs. Figure 1 depicts the specimen preparation and experimental process.

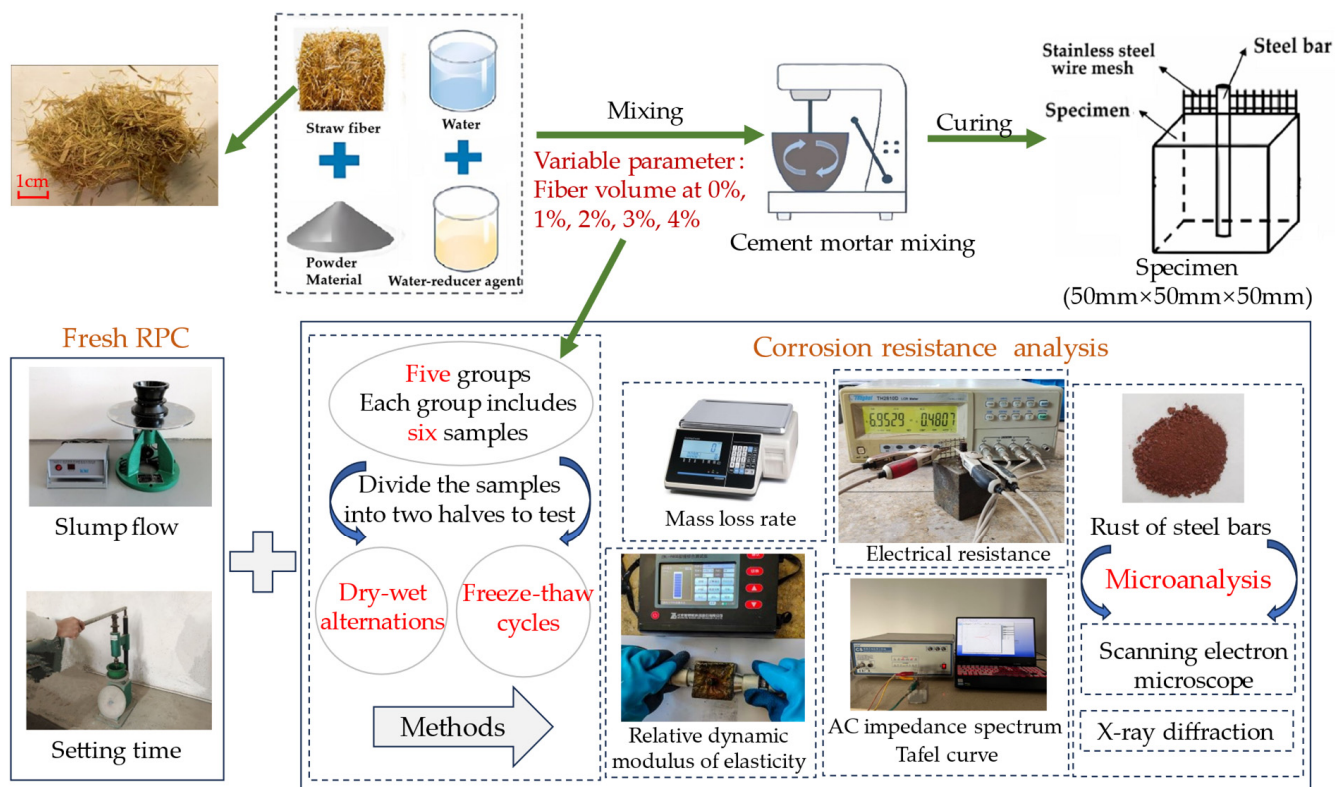


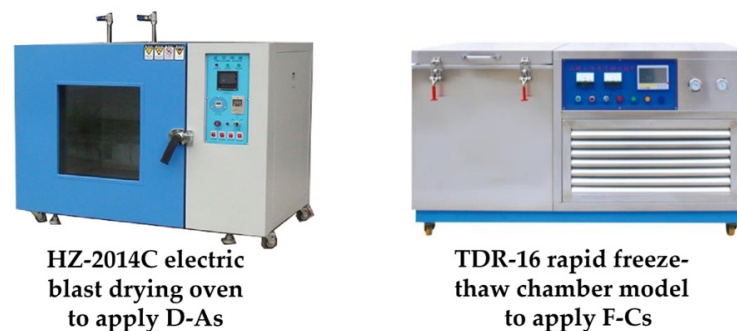
**Figure 1.** Specimen preparation and experimental process.

**Table 2.** The mix ratios of straw-fiber-reinforced RPC (kg/m<sup>3</sup>).

Group	Water	Cement	Silica Fume	Sand	Water Reducer	Straw Fibers
0	339.6	1018.9	339.6	679.2	26.4	0
1	339.6	1018.9	339.6	679.2	26.4	0.35
2	339.6	1018.9	339.6	679.2	26.4	0.70
3	339.6	1018.9	339.6	679.2	26.4	1.05
4	339.6	1018.9	339.6	679.2	26.4	1.40

## 2.2. Experimental Environment

In D-As, the specimens were dried in an HZ-2014C electric blast drying oven (manufactured by Dongguan Lixian Instrument Technology Co., Ltd., Dongguan, China) at 80 °C for 24 h. Then, they were cooled to 20 °C for 2 h and fully immersed in 3% NaCl solutions for 12 h at an ambient temperature. This process was repeated 10 times to complete the D-As. Furthermore, a TDR-16 rapid freeze-thaw chamber model (supplied by Hebei Dahong Experimental Instrument Co., Ltd., Cangzhou, China) was used to apply F-Cs. The experimental temperature was set to a range of −18 to 8 °C. Each cycle consisted of 3 h of freezing and thawing, which was repeated 100 times to complete the F-Cs. Figure 2 shows the electric blast drying oven and rapid freeze-thaw chamber model.

**Figure 2.** Machines to apply D-As and F-Cs.

## 2.3. Test Methods

The slump flow of fresh RPC refers to the GB/T2419-2005 standard [40]. The setting time was determined according to the standard JGJ 70-90 [41]. Each group of specimens was tested according to the above methods.

The mass loss rates (MLRs) of RPC specimens were calculated using Equation (1). In Equation (1),  $m_1$  is defined as the mass of the specimen after four days of immersion in 3% NaCl solutions (when the water on its surface has been wiped off), while  $m_t$  represents the mass of the specimen after exposure to different numbers of D-As or F-Cs.

$$MLR = \frac{m_t - m_1}{m_1} \times 100\% \quad (1)$$

The relative dynamic modulus of elasticity (RDME) was measured to reflect the internal defects of specimens [42]. The ZBL-F800 ultrasonic detector (accuracy up to 0.001 km/s, manufactured by Beijing Zhongbo Science and Technology Co., Ltd., Beijing, China) was utilized to determine the RDME. The RDME was obtained by following Equation (2), and the details are described in the GB/T 23900-2009 standard [43]. In Equation (2),  $v_1$  is the initial ultrasonic velocity of the specimen before D-A and F-C actions, while  $v_t$  represents the ultrasonic velocity of the specimen after exposure to certain numbers of D-As or F-Cs.

$$RDME = \left( \frac{v_t}{v_1} \right)^2 \times 100\% \quad (2)$$



The electrical resistance ( $R$ ) of RPC specimens was tested using a TH2810D LCR digital bridge. Furthermore, a two-electrode system was applied for the AC impedance spectrum (ACIS) testing. The working electrode was connected to the steel bar, while the counter electrode was connected to the stainless steel wire mesh. After D-As and F-Cs, the ACIS was measured using the CHI600E electrochemical workstation (Shanghai Chenhua Instrument Co., Ltd., Shanghai, China), and the scanning frequency range was set from 1 Hz to 100 kHz; the test voltage was set from  $-10$  to  $10$  mV. The Tafel curves were tested from  $-0.25$  to  $0.25$  V, with a step height of  $5$  mV and a step time of  $0.5$  s. Specific measurements can be found in Wang's study [44]. Corrosion rate and depth can be obtained using Equation (3), which refer to previous research [45]. In Equation (3),  $v$  and  $d$  are the corrosion area rate ( $\text{g}/\text{m}^2\text{h}$ ) and the corrosion depth ( $\text{mm}/\text{year}$ ), respectively.  $i_{\text{corr}}$  is the corrosion current density ( $\text{A}/\text{cm}^2$ ).  $M$  is the gram atomic weight ( $\text{g}$ ) of the metal, taken as  $M_{\text{Fe}} = 56$  g.  $\rho$  is the density of the metal ( $\text{g}/\text{cm}^3$ ), taken as  $\rho_{\text{Fe}} = 7.8$   $\text{g}/\text{cm}^3$ .  $n$  represents the ionic valence number, while  $F$  is the Faraday constant.

$$v = \frac{M}{nF} i_{\text{corr}} = 3.73 \times 10^{-4} \frac{M}{n} i_{\text{corr}}$$

$$d = \frac{v}{\rho} = 3.28 \times 10^{-3} \frac{M}{n\rho} i_{\text{corr}} \quad (3)$$

Figure 3 shows the test process of  $R$ , ACIS, and Tafel.

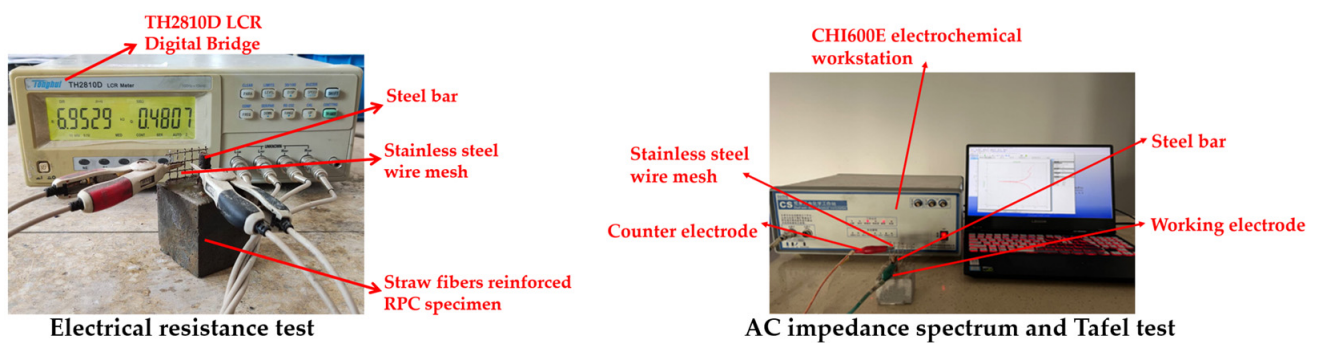


Figure 3. Specimen with electrical parameters being tested.

After 10 D-As and 100 F-Cs, the rebars of each group were removed from the RPC and the rust on its surface was scraped by an angle grinder. The collected rust was covered in plastic wrap and dried in the HZ-2014C electric blast drying oven for 2 h to conduct an SEM test using the Apreo-2 scanning electron microscope. After the SEM test, the rust was immediately tested by XRD. A total of 10 g of rust was ground into a fine powder to increase diffraction intensity. The scanning speed was set to  $1.2^\circ/\text{min}$  and the scanning range was  $20^\circ$ – $80^\circ$ . The XRD data were analyzed using MDI JADE software (version 6.5).

### 3. Results and Discussion

#### 3.1. Slump Flow and Setting Time

Figure 4 shows the slump flow and setting time of fresh RPC with straw fibers. The decreasing rate of slump flow was proportional to the fibers' volume, which decreased by 12.89% at 4% fibers. Straw fibers have good water absorption, which lowers the water–cement ratio and reduces the slurry's flowability. Furthermore, more cement paste surrounds the fibers due to their large surface area [46]. When the slurry is insufficient, it will lead to the deterioration of concrete workability and a decrease in fluidity. The error bars' values are lower than 5.9% of the slump flow's real values, showing the measuring accuracy.

The setting time of fresh RPC was reduced by 16.92% at 1% fiber volume and gradually increased thereafter, probably because more straw fibers hindered the contact and hydration

reaction between cement particles [47]. Longer straw fibers are more likely to be knotted and entangled with cement paste, which may reduce the fluidity. In this study, the average length of the straw fiber was treated at about 3 cm, which was conducive to its uniform dispersion during the mixing process. The working feasibility of fresh RPC with straw fibers was changed in a reasonable range.

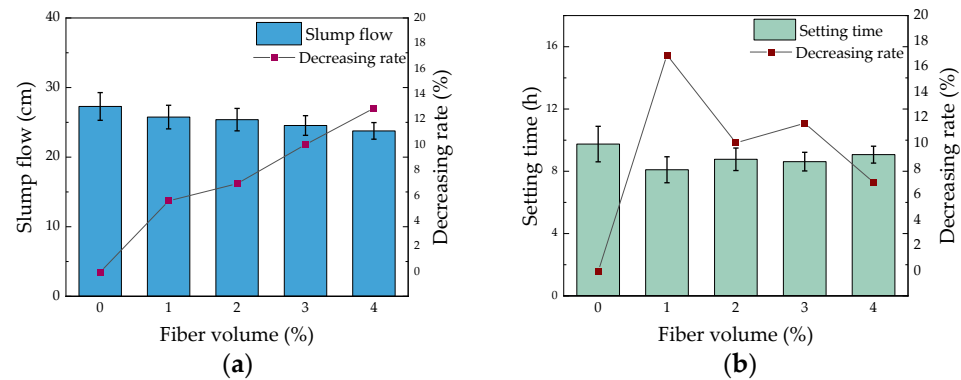


**Figure 4.** (a) Slump flow of fresh RPC; (b) setting time of fresh RPC.

### 3.2. The Mass Loss Rate

The mass loss rates of specimens in D-A and F-C actions are shown in Figure 5. During the D-As, the MLR of each group ranged from  $-0.2\%$  to  $-0.43\%$ . The surface of a straw fiber is scattered with closely spaced, delicate barb structures that enable it to fully connect with the cement slurry, forming a paste envelope, which prolongs the cement hydration reaction process. As hydration continues, more trace hydration products are generated [48]. Additionally, straw fibers possess good water absorption properties, which allow water and chlorides to introduce cracks and be absorbed by the fibers, resulting in an overall increase in the mass of the specimens [49]. The MLRs in F-Cs showed a positive correlation with the straw fibers, and the lowest was  $0.42\%$  at  $4\%$  fiber volume. The cement slurry and aggregate will shrink at low temperatures, while the water in the pores will expand in volume. Repeated freezing and thawing causes NaCl to penetrate the concrete, resulting in the precipitation and dissolution of the salt and the development of fine cracks, ultimately leading to a reduction in mass [50]. Sufficient straw fibers formed a spatial network structure and mechanical occlusion within the RPC, effectively reducing crack propagation and protecting the steel bar from oxidization.

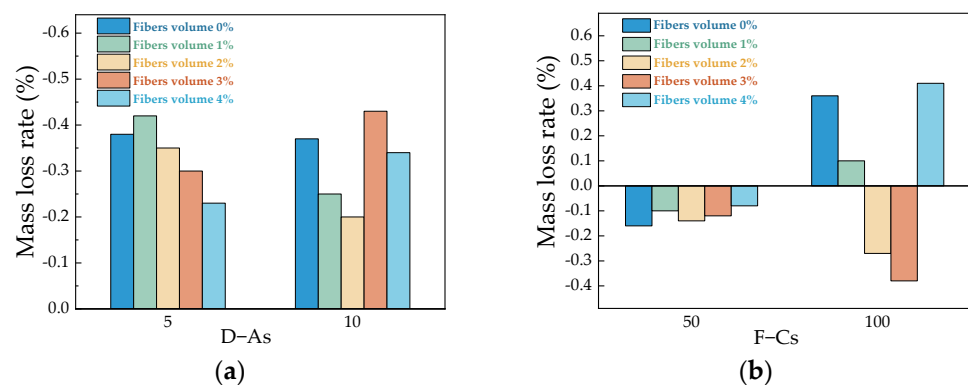


**Figure 5.** (a) Mass loss rate in D-As; (b) mass loss rate in F-Cs.

### 3.3. Relative Dynamic Modulus of Elasticity

Figure 6 displays the RDMEs of specimens subjected to two actions. In D-As, the decreasing rate of RDME showed a quadratic relationship with fiber volume, which may have been caused by the fact that the straw fibers in some specimens were connected into

clusters [51]. In addition, the RDMEs of the specimens mixed with straw fibers were higher by 9.34%–13.94% and 3.01%–5.26% when subjected to 10 D-As and 100 F-Cs, respectively. This suggests that the internal defects of the straw-fiber-reinforced RPC were modified, leading to less ultrasonic velocity loss. RPC and straw fibers create a good chemical bond and mechanical bite to form a cohesive assembly that inhibits cracking of the specimen [52]. The RDME of each group decreases with increasing cycles, and the reason for this is that the stress caused by the expansion of corrosion products, such as ettringite and gypsum, leads to the expansion of internal cracks and blocks the propagation of ultrasound [53]. The error bars associated with the RDME values are consistently below 7.5% of the total RDME, affirming the accuracy of the measurements.

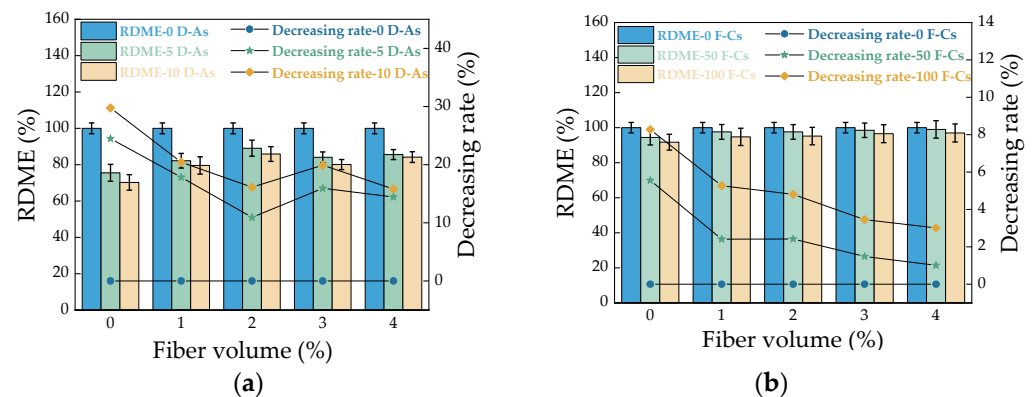


Figure 6. (a) RDMEs in D-As; (b) RDMEs in F-Cs.

### 3.4. Electrical Resistance

Figure 7 shows the  $R$  value and its decreasing rate in D-As and F-Cs. The  $R$  of each group significantly declined after five D-As. It might have been reduced due to the high ionic concentration of chloride salts that penetrated the interior of the specimens, which enhanced the ionic mobile conductivity [54]. In addition, the low fiber volume (1%–2%) had no apparent effect on the corrosion resistance of the specimens. The strong water absorption of straw fibers causes them to repeatedly expand and shrink during the D-A period. This phenomenon prevents some gaps from being filled, allowing chloride ions to penetrate more easily. This, in turn, reduces the electrical resistivity between the negative and positive poles of the steel bar, accelerating the electrochemical corrosion process [55]. In contrast, the  $R$  values in F-Cs were much higher than those of D-As. The corrosion of RPC specimens during D-As was more severe due to the longer test period. Furthermore, straw fibers could capture harmful impurities and chloride ions from the cracks in the concrete during F-Cs, minimizing their accumulation on the surface of the rebar's passivation film [56]. This improved the protection of the steel bar.

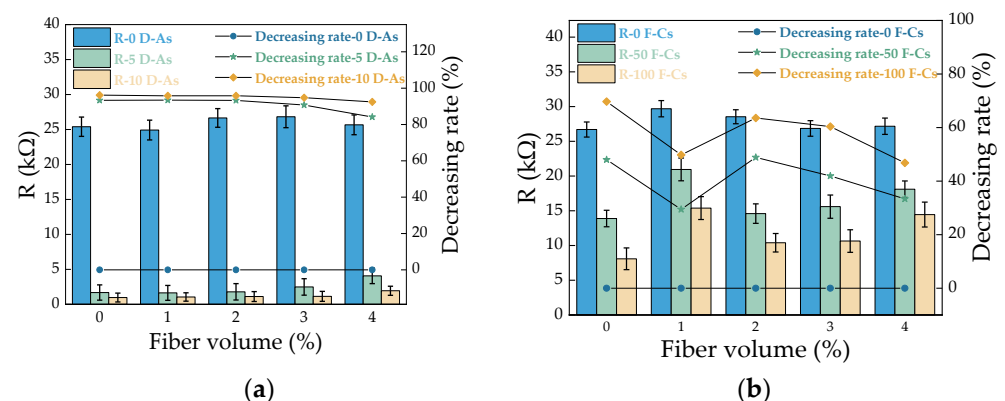
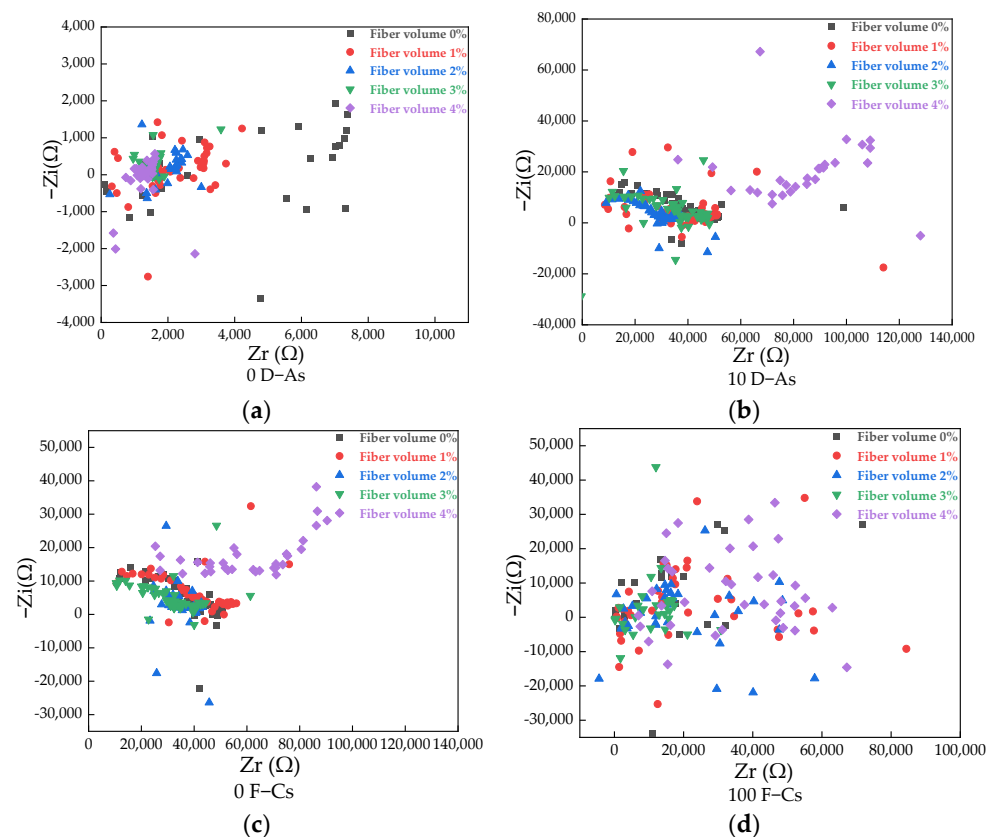


Figure 7. (a) Electrical resistance in D-As; (b) electrical resistance in F-Cs.

### 3.5. AC Impedance Spectrum

Figure 8a,b show the ACIS in D-As. It was observed that the impedance values of all groups were relatively high. This is because the free ions driven by the electric field in the cement matrix tend to move towards the interface between the electrode and the steel bar, forming an ionic double layer, while the reaction at the interface of the steel bar was slow, and the charge could not migrate to the ionic conductor in time and accumulate on the electrode surface, resulting in a huge polarization resistance on the impedance spectrum [57,58]. After 10 D-As, the image was shifted towards the right. At 4% fiber volume, it had a higher capacitive impedance than the others, which means that electrons are harder to transfer, indicating better corrosion resistance. Figure 8c,d show the ACIS in F-Cs. They show a smaller decrease in both the imaginary and real parts compared with those of D-As. In addition, there is a random distribution of points in all groups, which was caused by the polarization effect as well as the enhanced movement of ions in the liquid phase. The movement speed of electrons was greater than the electrode reaction speed, and the fast electron outflow caused the anode positive charge accumulation, and its electrode potential was shifted in the positive direction [59]. Meanwhile, the electron inflow on the cathode was fast, and the accumulation of negative charge resulted in a shift of the electrode potential in the negative direction. The electrode potential deviated from the equilibrium state, forming an inverse electric field that hindered the movement of electrons and made the specimens less conductive. The straw fibers absorbed a large amount of solution, as the specimens were in a water-saturated state, which strengthened the liquid-phase ion movement, resulting in an increase in electrical conductivity and a decrease in the  $R$  value [60]. Due to the coupling of these two factors, the electrochemical stability was affected, causing many discrete points to appear. The ACIS at 4% fiber volume is obviously located on the right side of other groups. It indicates that the resistance to electrochemical corrosion of specimens is improved by straw fibers.



**Figure 8.** (a) ACIS of 0 D-As; (b) ACIS of 10 D-As; (c) ACIS of 0 F-Cs; (d) ACIS of 100 F-Cs.



The equivalent circuit diagram of the impedance curve above can be obtained by using impedance spectrum fitting software, ZSimp-Win3.5. The fitting process can refer to the previous study [61]. The result is shown in Figure 9, and the Chi values of equivalent circuits were all lower than 0.01, indicating the fitting accuracy. It is comprised of four interconnected components arranged in series.  $R_s$  represents the contact resistance between electrodes and specimen, while  $R_i$  ( $i = 1, 2, 3$ ) denotes the resistance of the pore solution, the interface between the cement matrix and the cementitious phase, and the rust, which are connected in parallel with the capacitive element  $C_i$  ( $i = 1, 2, 3$ ), respectively [62,63].

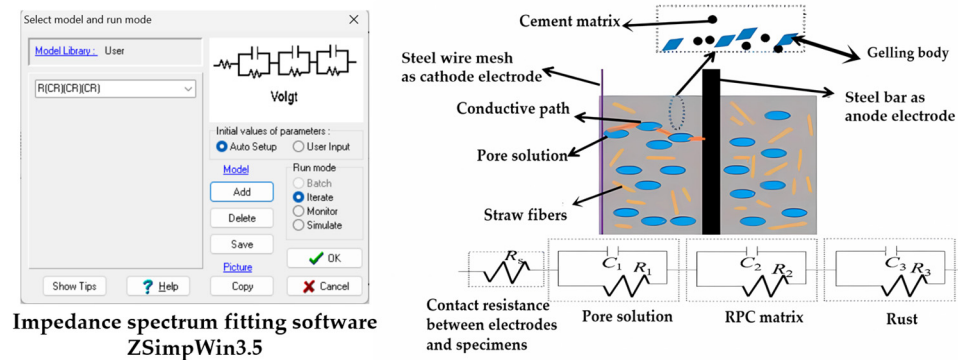


Figure 9. Equivalent circuit diagram of the RPC specimen.

### 3.6. Corrosion Rate and Corrosion Depth

Figure 10a,c show the Tafel curves under 10 D-As and 100 F-Cs, respectively. The corrosion depth of steel bars that are fully immersed in seawater ranges from 0.09 to 0.201 mm/year [64]. However, the concrete at the interface between seawater and air is usually subjected to D-As and F-Cs, which results in a more pronounced corrosion phenomenon due to the repeated infiltration of chloride ions into the cracks and subsequent damage to the steel bars [65]. This is consistent with the experimental results shown in Figure 10b,d. The corrosion rates and depths in two cycles exhibited quadratic functions with fiber content, with the lowest values observed at 4% fiber volume, which decreased by 33.4% and 49.8% in D-As and F-Cs, respectively. When immersed in NaCl solutions, the concrete will absorb water until it reaches a saturated state due to capillary adsorption. After drying, water evaporates from the concrete, creating an ion concentration difference between the inside and outside [66]. Chloride in the pores then diffuses inside along the concentration gradient, causing damage to accumulate repeatedly [67]. Straw fibers can serve as the filler to patch cracks and improve permeability resistance. Additionally, straw fibers cannot react chemically with chloride ions, which is beneficial for reducing the corrosion rate.

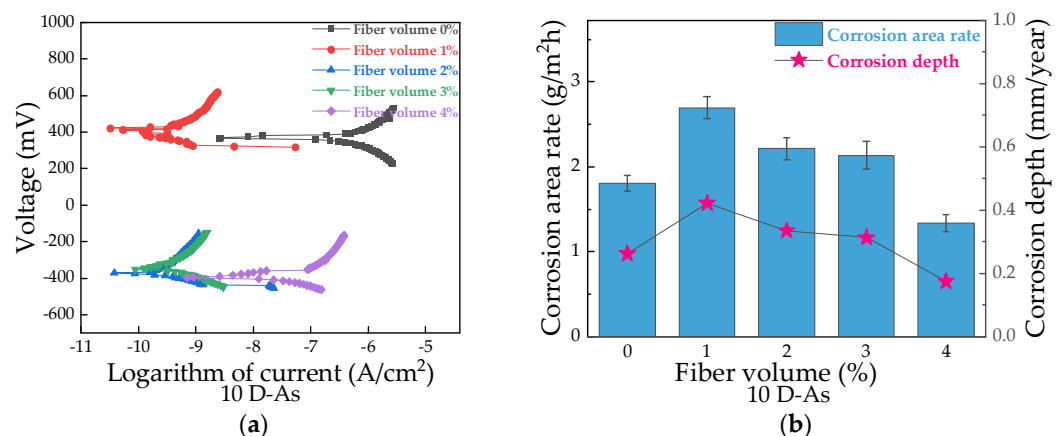
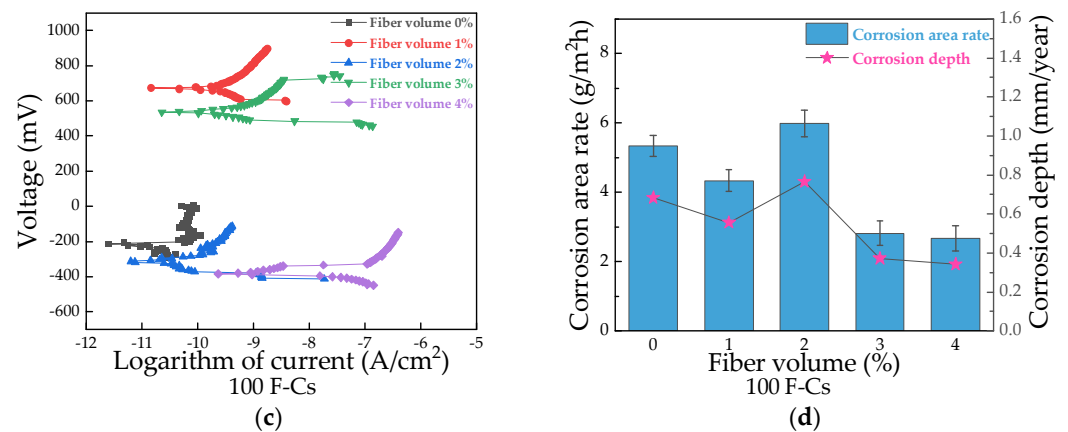


Figure 10. Cont.



**Figure 10.** (a) Tafel curves of 10 D–As; (b) corrosion rate and depth in 10 D–As; (c) Tafel curves of 100 F–Cs; (d) corrosion rate and depth in 100 F–Cs.

### 3.7. Scanning Electron Microscopy and Energy Dispersive Spectrometer

Electrical test results show that 4% of straw fibers can provide the best corrosion resistance. After 10 D-As and 100 F-Cs, the rebar rust of groups with 0% and 4% fibers were scraped for SEM-EDS analysis to compare the oxidation corrosion. Figure 11 shows four groups of SEM scanning images of the rebar rust. The main elements according to the EDS test are also listed in Table 3.

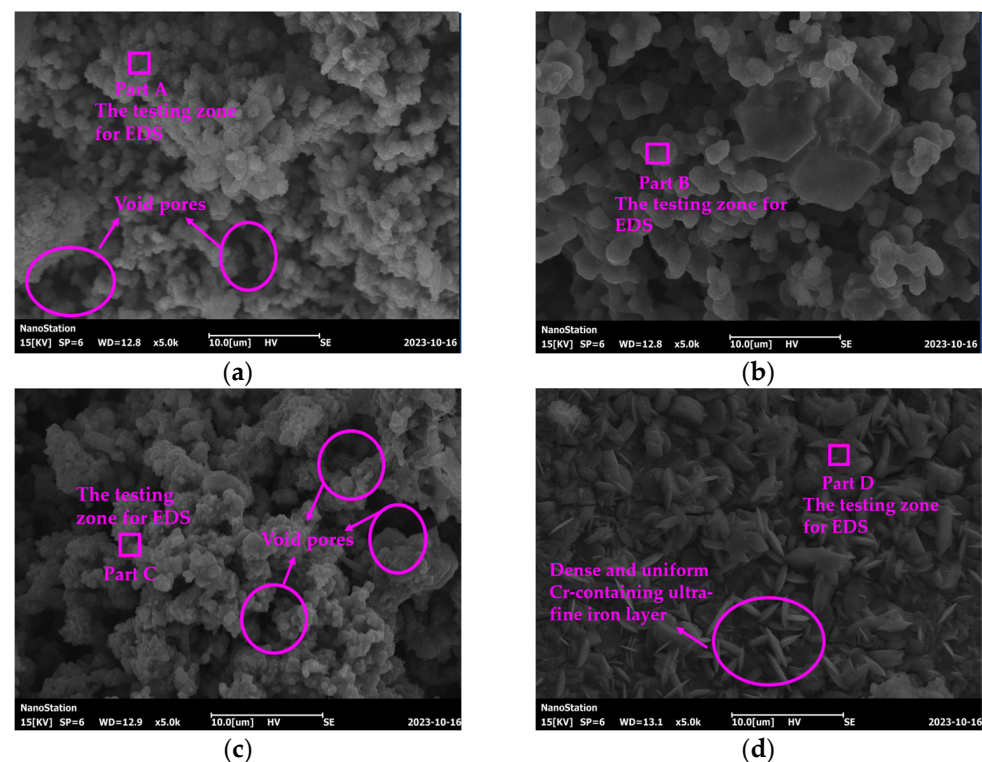


**Figure 11.** (a) Rust of 0% fiber RPC in 10 D–As; (b) rust of 4% fiber RPC in 10 D–As; (c) rust of 0% fiber RPC in 100 F–Cs; (d) rust of 4% fiber RPC in 100 F–Cs.

There are bigger and more numerous voids in the rust of the 0% fibers group, which creates more possibilities for oxygen and chloride ions to aggravate the corrosion of the steel bars. In Figure 11d, it can be observed that a dense and uniform Cr-containing ultra-fine iron layer forms after 100 F-Cs, and the protective rust layer inhibits further oxidation reaction, indicating that straw fibers effectively improve the corrosion resistance of steel bars [68]. As shown in Figure 11b, D-A actions last longer than F-Cs and are more

susceptible to chloride invasion; the corrosion of rebars is more serious, which is also consistent with the resistance change trend in the previous results [69,70]. The main factors affecting the density of the rust layer are the fiber volume and the cycle types.

**Table 3.** The main elements in different parts (wt.%).

Part	C	O	Na	Cl	Fe	Ni	Cr	Ca	K
A	1.33	45.60	2.08	1.85	44.05	0.29	0.48	2.31	-
B	1.63	26.17	2.69	1.35	62.98	1.55	2.32	1.31	-
C	-	36.24	4.66	2.88	55.32	-	0.47	0.20	0.23
D	-	23.79	3.04	2.46	66.42	0.44	3.49	0.37	-

The corrosion resistance of iron is related to the structure of the rust layer, which depends on the types and content of elements in the rust layer [71,72]. It can be seen from Table 3 that the Fe/O value of the 0% fiber RPC under D-As is the lowest, indicating that the weight percentage of oxygen element in the rust is the highest. In the oxide, the higher the proportion of oxygen element, that is, the higher the oxidation state, the higher the degree of oxidation [73]. The Fe/O of 4% fiber RPC is above 2.4, which suggests that the rust has experienced less oxidative corrosion than 0% fiber RPC, and its oxides may contain  $\text{Fe}_2\text{O}_3$  (Fe/O = 112/48),  $\text{Fe}_3\text{O}_4$  (Fe/O = 168/64), other hydroxides, and amorphous substances. The percentage of chlorine element indicates that the amount of chloride in the 4% fiber RPC is lower than at the 0% fiber volume, which proves that straw fibers enhance the corrosion resistance.

### 3.8. X-ray Diffraction

After SEM-EDS, the rusts of four groups above were tested by X-ray diffraction. Figure 12 displays the XRD pattern of the rusts. The peak of XRD is mainly the oxides of Fe, including  $\alpha\text{-FeO(OH)}$ ,  $\beta\text{-FeO(OH)}$ ,  $\text{Fe}_3\text{O}_4$ , and  $\text{Fe}_2\text{O}_3$ , and the mass fraction of each phase changes little. The peaks of  $\text{Fe}_3\text{O}_4$  and  $\text{Fe}_2\text{O}_3$  almost overlap in the spectrum, which may be due to the relatively slow oxidation corrosion rate of rust [74], so that oxygen is fully involved in the corrosion reaction of the rebars. There was more  $\beta\text{-FeO(OH)}$  in groups without straw fibers. The absence of straw fibers to fill the pores inside the RPC resulted in enhanced oxygen diffusion in the electrolyte solution. Consequently, the  $\text{Fe}^{2+}$  in the  $\beta\text{-FeO(OH)}$  lattice would be oxidized to  $\text{Fe}^{3+}$ , thereby accelerating corrosion [75]. However,  $\alpha\text{-FeO(OH)}$  was observed after adding straw fibers, which have greater density and protective properties, effectively preventing the corrosive medium from transferring to the interior of the rebars [76]. The formation of  $\alpha\text{-FeO(OH)}$  is similar to that of galvanized coated steel bars, indicating better corrosion resistance [77]. The peak of XRD in groups with straw fibers is more obvious, possibly because the rust in this case contains more goethite [78].

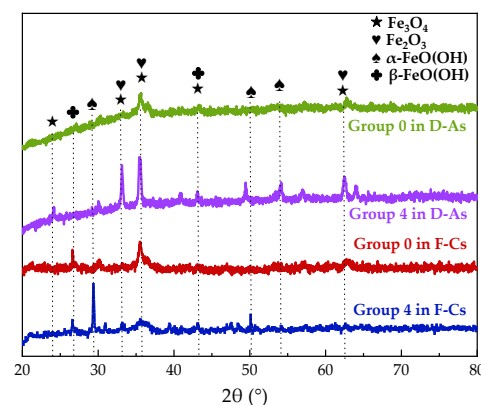


**Figure 12.** XRD pattern of the rusts.

#### 4. Conclusions

In this study, the effect of straw fibers on the working feasibility and corrosion resistance of reinforced RPC was investigated. The optimum volume of straw fibers was 4%, which was also verified by SEM-EDS and XRD tests. The conclusions are as follows:

- (1) After adding straw fibers, the setting time and slump flow of fresh RPC were reduced by up to 16.92% and 12.89%. In D-A and F-C actions, the MLRs in D-As and F-Cs were  $-0.44\%$ – $-0.43\%$  and  $-0.38\%$ – $-0.42\%$ , respectively. The RDMEs of RPC specimens were improved by 9.34%–13.94% and 3.01%–5.26%, while the R was improved by 3.73% and 22.90%, respectively. The corrosion rates and depths of rebars were lowest at 4% fiber volume, which were 1.3356 g/m<sup>2</sup>h, 0.1745 mm/year in D-As, 2.6732 g/m<sup>2</sup>h, 0.3427 mm/year in F-Cs.
- (2) The corrosion resistance of rebars inside RPC was strengthened by straw fibers, as evidenced by fewer void pores and the uniform, ultra-fine iron surface layer. Additionally,  $\alpha$ -FeO(OH) was observed, and its dense oxidized layer prevented further chemical reaction between the chloride ions and steel bars.
- (3) The corrosion potential of RPC was enhanced by the addition of straw fibers, which inhibited the polarization reaction in NaCl solutions. The degree of corrosion was correlated with the types of cycle action and fiber volumes. The electrochemical phenomena indicated that straw fibers could be used as a protective coating material for concrete under chloride environments.

**Author Contributions:** Conceptualization, W.S. and Y.J.; methodology, A.W.; software, A.W.; validation, W.S. and M.L.; formal analysis, A.W.; investigation, A.W. and H.W.; resources, Y.J.; data curation, H.W.; writing—original draft preparation, A.W.; writing—review and editing, A.W., X.P., M.L. and H.W.; visualization, A.W. and H.W.; supervision, M.L., X.P. and H.W.; project administration, W.S., X.P. and H.W.; funding acquisition, H.W. and X.P. All authors have read and agreed to the published version of the manuscript.

**Funding:** This research was supported by Zhejiang Provincial Natural Science Foundation of China (No. LY22E080005, No. LY24E080010).

**Institutional Review Board Statement:** Not applicable.

**Informed Consent Statement:** Not applicable.

**Data Availability Statement:** The data used to support the findings of this study are available on request.

**Conflicts of Interest:** Authors Weixiang Sun and Miao Lu were employed by the China Construction Infrastructure Co., Ltd. Author Xi Peng was employed by the company Ningbo Roaby Technology Industrial Group Co., Ltd. The remaining authors declare that the research was conducted in the absence of any commercial or financial relationships that could be construed as a potential conflict of interest.

#### References

1. Sanjuán, M.Á.; Andrade, C. Reactive powder concrete: Durability and applications. *Appl. Sci.* **2021**, *11*, 5629. [\[CrossRef\]](#)
2. Dhundasi, A.; Khadiranaikar, R.; Momin, A. An experimental investigation on durability properties of reactive powder concrete. *Int. J. Eng. Sci.* **2022**, *35*, 327–336.
3. Ma, F.; Deng, M.; Ma, Y. Experimental study on interior precast concrete beam–column connections with lap-spliced steel bars in field-cast RPC. *Eng. Struct.* **2021**, *228*, 111481. [\[CrossRef\]](#)
4. Al-Quraishi, H.; Al-Farttoosi, M.; AbdulKhudhur, R. Tension lap splice length of reinforcing bars embedded in reactive powder concrete (RPC). *Structures* **2019**, *19*, 362–368. [\[CrossRef\]](#)
5. Wang, D.; Han, L.; Ju, Y.; Zeng, C. Bond behavior between reinforcing bar and reactive powder concrete. *Struct. Concr.* **2022**, *23*, 2630–2642. [\[CrossRef\]](#)
6. Wang, X.; Dong, S.; Ashour, A.; Ding, S. Bond behaviors between nano-engineered concrete and steel bars. *Constr. Build. Mater.* **2021**, *299*, 124261. [\[CrossRef\]](#)
7. Yi, T.; Wang, H.; Xie, J.; Wang, W. Flexural strength and acoustic damage characteristics of steel bar reactive powder concrete. *Appl. Sci.* **2021**, *11*, 7017. [\[CrossRef\]](#)

8. Ju, Y.; Zhao, J.; Wang, D.; Song, Y. Experimental study on flexural behaviour of reinforced reactive powder concrete pole. *Constr. Build. Mater.* **2021**, *312*, 125399. [\[CrossRef\]](#)
9. Deng, M.; Ma, F.; Ye, W.; Li, F. Flexural behavior of reinforced concrete beams strengthened by HDC and RPC. *Constr. Build. Mater.* **2018**, *188*, 995–1006. [\[CrossRef\]](#)
10. Taheri-Shakib, J.; Al-Mayah, A. Effect of corrosion pit distribution of rebar on pore, and crack characteristics in concrete. *Cem. Concr. Compos.* **2024**, *148*, 105476. [\[CrossRef\]](#)
11. Li, S.; Jin, Z.; Chang, H.; Gao, Y. Oxygen diffusion into unsaturated seawater and sea sand concrete and its effect on non-uniform corrosion of steel bars. *J. Build. Eng.* **2024**, *84*, 108665. [\[CrossRef\]](#)
12. Qian, R.; Li, Q.; Fu, C.; Zhang, Y.; Wang, Y.; Jin, X. Atmospheric chloride-induced corrosion of steel-reinforced concrete beam exposed to real marine-environment for 7 years. *Ocean Eng.* **2023**, *286*, 115675. [\[CrossRef\]](#)
13. Zeng, C.; Zheng, Z.; Zhang, H.; Wang, X.; Liu, G. 3D mesoscale investigation of non-uniform steel corrosion in reinforced concrete under chloride environments. *Constr. Build. Mater.* **2024**, *411*, 134273. [\[CrossRef\]](#)
14. Kingsley, U.; Efeeloo, N.; Kennedy, C. Evaluation of Residual Structural Capacity in Corroded Reinforced Concrete Structures. *J. Eng. Technol.* **2024**, *4*, 54–70. [\[CrossRef\]](#)
15. Men, P.; Ho, H.; Zhou, X.; Chung, K. Experimental investigations into stocky composite columns of concrete-filled circular S690 steel tubes under compression. *Eng. Struct.* **2024**, *309*, 118016. [\[CrossRef\]](#)
16. Fang, X.; Pan, Z.; Chen, A.; Tian, H.; Ma, R. Phase-field method for modeling non-uniform corrosion-induced cracking in concrete. *Eng. Fract. Mech.* **2023**, *281*, 109131. [\[CrossRef\]](#)
17. Mansour, M.; Ismail, M.H.; Latif, L.; Alshalif, A.; Milad, A.; Bargi, W. A systematic review of the concrete durability incorporating recycled glass. *Sustainability* **2023**, *15*, 3568. [\[CrossRef\]](#)
18. Hesam, D.; Marta, R.; Pedro, S. Self-healing efficiency of Ultra High-Performance Fiber-Reinforced Concrete through permeability to chlorides. *Constr. Build. Mater.* **2021**, *310*, 125168.
19. Wang, T.; Xu, J.; Meng, B.; Peng, G. Experimental study on the effect of carbon nanofiber content on the durability of concrete. *Constr. Build. Mater.* **2020**, *250*, 118891. [\[CrossRef\]](#)
20. Miyazato, S.; Hiraishi, Y. Durability against steel corrosion of HPFRCC with bending cracks. *J. Adv. Concr. Technol.* **2013**, *11*, 135–143. [\[CrossRef\]](#)
21. Fu, Q.; Xu, W.; Bu, M.; Guo, B.; Niu, D. Orthogonal experimental study on hybrid-fiber high-durability concrete for marine environment. *J. Mater. Res. Technol.* **2021**, *13*, 1790–1804. [\[CrossRef\]](#)
22. Zhang, G.; Liu, C.; Chen, P.; Li, Z.; Han, Y. Enhancing the interfacial compatibility and self-healing performance of microbial mortars by nano-SiO<sub>2</sub>-modified basalt fibers. *Cem. Concr. Compos.* **2024**, *152*, 105650. [\[CrossRef\]](#)
23. Men, P.; Wang, X.; Liu, D.; Zhang, Z.; Lu, Y. On use of polyvinylpyrrolidone to modify polyethylene fibers for improving tensile properties of high strength ECC. *Constr. Build. Mater.* **2024**, *417*, 135354. [\[CrossRef\]](#)
24. Singh, A.K.; Bedi, R.; Khajuria, A. A review of composite materials based on rice straw and future trends for sustainable composites. *J. Clean. Prod.* **2024**, *457*, 142417. [\[CrossRef\]](#)
25. Wu, B.; Zhang, S.; Zhao, Y. Dynamic compressive properties of rubberized mortar reinforced with straw-fiber additive. *Constr. Build. Mater.* **2023**, *408*, 133679. [\[CrossRef\]](#)
26. Rajput, A.; Gupta, S.; Bansal, A. A review on recent eco-friendly strategies to utilize rice straw in construction industry: Pathways from bane to boon. *Environ. Sci. Pollut. Res.* **2023**, *30*, 11272–11301. [\[CrossRef\]](#) [\[PubMed\]](#)
27. Liu, J.; Zhao, W.; Li, L. Effects of Nano-SiO<sub>2</sub> grafting on improving the interfacial and mechanical properties of concrete with rice straw fibers. *Constr. Build. Mater.* **2023**, *398*, 132516. [\[CrossRef\]](#)
28. Farooqi, M.U.; Ali, M. Durability evaluation of wheat straw reinforced concrete for sustainable structures. *J. Build. Eng.* **2024**, *82*, 108400. [\[CrossRef\]](#)
29. Basta, A.H.; Lotfy, V.F.; Shafik, E.S. Synergistic Valorization of Rice Straw and Red Brick Demolition in development performance of Lightweight Cement Mortars. *J. Build. Eng.* **2024**, *92*, 109769. [\[CrossRef\]](#)
30. Gong, K.; Liang, Z.; Peng, X.; Wang, H. Research into Preparation and Performance of Fast-Hardening RPC Mixed with Straw. *Materials* **2023**, *16*, 5310. [\[CrossRef\]](#)
31. Mahdy, M.M.; Mahfouz, S.Y.; Tawfic, A.F.; Ali, M. Performance of rice straw fibers on hardened concrete properties under effect of impact load and gamma radiation. *Fibers* **2023**, *11*, 42. [\[CrossRef\]](#)
32. Ahmad, J.; Mohammed, J.; Tayyab, N.M. Improvement in the strength of concrete reinforced with agriculture fibers: Assessment on mechanical properties and microstructure analysis. *J. Eng. Fibers Fabr.* **2024**, *19*, 1226480. [\[CrossRef\]](#)
33. Beskopylny, A.N.; Stelmakh, S.A.; Shcherban, E. Influence of Electromagnetic Activation of Cement Paste and Nano-Modification by Rice Straw Biochar on the Structure and Characteristics of Concrete. *J. Compos. Sci.* **2022**, *6*, 268. [\[CrossRef\]](#)
34. Moussi, Y.; Clerc, L.; Benezet, J.C. Study of the Impact of Rice Straw Particle Size on the Mechanical and Thermal Properties of Straw Lime Concretes. *J. Archit. Eng.* **2022**, *1*, 361–368.
35. Zhao, R.; Feng, B.; Fu, J. Study on Improving Physical–Mechanical Properties and Frost Resistance of Straw–Mortar Composite Wall Materials by Pretreatment. *Sustainability* **2024**, *16*, 5608. [\[CrossRef\]](#)
36. Nafea, A.; Elrahman, A.M.; Ghonaim, S.A. Behavior of Natural Fiber Reinforced Concrete Using Rice Straws. *J. Archit. Eng.* **2021**, *6*, 26–32.



37. Qi, W.; Zhang, S.; Fang, Z.; Zheng, J. Effect of maintenance environment on the mechanical property and pore structure of cement paste mixed by seawater. *Constr. Build. Mater.* **2024**, *418*, 135280. [\[CrossRef\]](#)
38. GB/T 50081-2019; Standard for Test Methods of Concrete Physical and Mechanical Properties. Ministry of Housing and Urban-Rural Development, People's Republic of China: Beijing, China, 2019.
39. GB/T 50204-2015; Code for Acceptance of Constructional Quality of Concrete Structures. Ministry of Housing and Urban-Rural Development, People's Republic of China: Beijing, China, 2015.
40. GB/T 2419-2005; Test Method for Fluidity of Cement Mortar. Ministry of Housing and Urban-Rural Development, People's Republic of China: Beijing, China, 2005.
41. JGJ/T 70-2009; Standard for Test Method of Basic Properties of Construction Mortar. Ministry of Housing and Urban-Rural Development, People's Republic of China: Beijing, China, 2009.
42. Zouini, R.; Makani, A.; Tafroui, A. Investigation on the mechanical properties and durability of high performance concrete reinforced with waste tires fibers. *J. Eng. Exact. Sci.* **2023**, *9*, 16062-01e. [\[CrossRef\]](#)
43. GB/T 23900-2009; Non-Destructive Testing—Practice for Measuring Ultrasonic Velocity in Materials. Standardization Administration of China, People's Republic of China: Beijing, China, 2009.
44. Wang, H.; Cai, X.; Peng, X. Study on Soil Corrosion Resistance Reinforced with Reactive Powder Concrete in Chloride Environment. *Coatings* **2023**, *13*, 1134. [\[CrossRef\]](#)
45. Elsener, B. Corrosion rate of steel in concrete—Measurements beyond the Tafel law. *Corros. Sci.* **2005**, *12*, 3019–3033. [\[CrossRef\]](#)
46. Feng, B.; Liu, J.; Lu, Z.; Zhang, M.; Tan, X. Study on properties and durability of alkali activated rice straw fibers cement composites. *J. Build. Eng.* **2023**, *63*, 105515. [\[CrossRef\]](#)
47. Shang, X.; Yang, J.; Song, Q.; Wang, L. Efficacy of modified rice straw fiber on properties of cementitious composites. *J. Clean. Prod.* **2020**, *276*, 124184. [\[CrossRef\]](#)
48. Jin, Z.; Mao, S.; Zheng, Y.; Liang, K. Pre-treated corn straw fiber for fiber-reinforced concrete preparation with high resistance to chloride ions corrosion. *Case Stud. Constr. Mater.* **2023**, *19*, e02368. [\[CrossRef\]](#)
49. Poorsaheli, H.; Behravan, A.; Aghda, S.T.; Gholami, A. A study on the durability parameters of concrete structures reinforced with synthetic fibers in high chloride concentrated shorelines. *Constr. Build. Mater.* **2019**, *200*, 578–585. [\[CrossRef\]](#)
50. Li, J.; Chang, J.; Qiao, H. Performance Degradation of Fiber-Reinforced Concrete under Freeze–Thaw Cycles and Its Resistance to Chloride Ion Penetration. *J. Mater. Civ. Eng.* **2022**, *34*, 04022180. [\[CrossRef\]](#)
51. Jiang, H.; Wang, K.; Wang, H. The Corrosion Resistance of Reinforced Reactive Powder Concrete with Secondary Aluminum Ash Exposed to NaCl Action. *Materials* **2023**, *16*, 5615. [\[CrossRef\]](#)
52. Farooqi, M.; Ali, M. Effect of pre-treatment and content of wheat straw on energy absorption capability of concrete. *Constr. Build. Mater.* **2019**, *224*, 572–583. [\[CrossRef\]](#)
53. Ongpeng, J.; Oreta, A.; Hirose, S. Characterization of damage using ultrasonic testing on different types of concrete. *Mater. Eval.* **2018**, *76*, 1532–1541.
54. Cosoli, G.; Mobili, A.; Tittarelli, F.; Revel, G.; Chiariotti, P. Electrical resistivity and electrical impedance measurement in mortar and concrete elements: A systematic review. *Appl. Sci.* **2020**, *10*, 9152. [\[CrossRef\]](#)
55. Chidiac, S.; Shafikhani, M. Electrical resistivity model for quantifying concrete chloride diffusion coefficient. *Cem. Concr. Compos.* **2020**, *113*, 103707. [\[CrossRef\]](#)
56. Sharma, T.; Singh, S. The experimental study on the effect of paddy straw fibers on mechanical properties of sustainable concrete. *J. Green Eng.* **2020**, *10*, 7997–8009.
57. Wang, R.; He, F.; Chen, C.; Dai, L. Evaluation of electrode-sample contact impedance under different curing humidity conditions during measurement of AC impedance of cement-based materials. *Sci. Rep.* **2020**, *10*, 17968. [\[CrossRef\]](#) [\[PubMed\]](#)
58. Ishai, P.B.; Talary, M.S.; Caduff, A.; Levy, E.; Feldman, Y. Electrode polarization in dielectric measurements: A review. *Meas. Sci. Technol.* **2013**, *24*, 102001. [\[CrossRef\]](#)
59. Zhang, J.; Heath, A.; Abdalgadir, H.; Richard, B.; Paine, K. Electrical impedance behaviour of carbon fibre reinforced cement-based sensors at different moisture contents. *Constr. Build. Mater.* **2022**, *353*, 129049. [\[CrossRef\]](#)
60. Li, Q.; Ibrahim, L.; Zhou, W.; Zhang, M.; Yuan, Z. Treatment methods for plant fibers for use as reinforcement in cement-based materials. *Cellulose* **2021**, *28*, 5257–5268. [\[CrossRef\]](#)
61. Wang, R.; Hu, Z.; Li, Y.; Wang, K.; Zhang, H. Review on the deterioration and approaches to enhance the durability of concrete in the freeze–thaw environment. *Constr. Build. Mater.* **2022**, *321*, 126371. [\[CrossRef\]](#)
62. Wang, D.; Xu, Z.Q.; Xu, N.; Hu, Z.; Wang, H.; Shi, F. The Corrosion Resistance of Concrete-Filled Steel Tubes with the Assembly Unit of Na<sub>2</sub>MoO<sub>4</sub> and Benzotriazole. *Coatings* **2024**, *14*, 349. [\[CrossRef\]](#)
63. Qiao, C.; Ni, W.; Wang, Q.; Weiss, J. Chloride diffusion and wicking in concrete exposed to NaCl and MgCl<sub>2</sub> solutions. *J. Mater. Civ. Eng.* **2018**, *30*, 04018015. [\[CrossRef\]](#)
64. Tian, Y.; Zhang, G.; Ye, H. Corrosion of steel rebar in concrete induced by chloride ions under natural environments. *Constr. Build. Mater.* **2023**, *369*, 130504. [\[CrossRef\]](#)
65. Chen, C.; Wang, L.; Liu, R. Chloride penetration of concrete exposed to dry-wet cycle with various dry-wet ratios and temperature. *Constr. Build. Mater.* **2023**, *400*, 132883. [\[CrossRef\]](#)
66. Xu, W.; Li, Y.; Li, H.; Wang, K.; Zhang, C. Corrosion mechanism and damage characteristic of steel fiber concrete under the effect of stray current and salt solution. *Constr. Build. Mater.* **2022**, *314*, 125618. [\[CrossRef\]](#)

67. Chen, J.; Jia, J.; Zhu, M. Development of admixtures on seawater sea sand concrete: A critical review on Concrete hardening, chloride ion penetration and steel corrosion. *Constr. Build. Mater.* **2024**, *411*, 134219. [[CrossRef](#)]
68. Deng, Q.; Wang, Z.; Li, S.; Yu, Q. Salt scaling resistance of pre-cracked ultra-high performance concrete with the coupling of salt freeze-thaw and wet-dry cycles. *Cem. Concr. Compos.* **2024**, *146*, 105396. [[CrossRef](#)]
69. Wang, R.; Zhang, Q.; Li, Y. Deterioration of concrete under the coupling effects of freeze–thaw cycles and other actions: A review. *Constr. Build. Mater.* **2022**, *319*, 126045. [[CrossRef](#)]
70. Wang, Y.; Li, J.; Zhang, L.; Wang, T. Structure of the rust layer of weathering steel in A high chloride environment: A detailed characterization via HRTEM, STEM-EDS, and FIB-SEM. *Corros. Sci.* **2020**, *177*, 108997. [[CrossRef](#)]
71. Mahram, K.; Ray, K.; Chen, L. Residual mechanical performance and rust characterization of self-prestressing UHPM subjected to chloride-induced corrosion. *Constr. Build. Mater.* **2023**, *398*, 132469.
72. Yashwantraj, S.; Wharton, J.; Baboo, Y. Mechanistic modelling of atmospheric corrosion of carbon steel in Port-Louis by electrochemical characterisation of rust layers. *Mater. Chem. Phys.* **2022**, *291*, 126694.
73. Bazán, A.; Gálvez, J.; Reyes, E.; Galé-Lamuela, D. Study of the rust penetration and circumferential stresses in reinforced concrete at early stages of an accelerated corrosion test by means of combined SEM, EDS and strain gauges. *Constr. Build. Mater.* **2018**, *184*, 655–667. [[CrossRef](#)]
74. Wang, G.; Wu, Q.; Li, X.; Xu, J.; Yao, X.; Shi, W.; Wang, S. Microscopic analysis of steel corrosion products in seawater and sea-sand concrete. *Materials* **2019**, *12*, 3330. [[CrossRef](#)]
75. Wang, P.; Chen, X.; Zhang, Z.; Huang, Y.; Ma, L. Roles of grain refinement in the rust formation and corrosion resistance of weathering steels. *Corros. Sci.* **2023**, *224*, 111561. [[CrossRef](#)]
76. Zhang, H.; Xu, J.; Guo, L.; Dong, H. Study on rust layers of carbon steel, weathering steel and alloy steel exposed to Shanghai atmosphere for three years. *Mater. Today Commun.* **2023**, *35*, 105520. [[CrossRef](#)]
77. Daniel, E.F.; Wang, C.; Li, C. Evolution of corrosion degradation in galvanised steel bolts exposed to a tropical marine environment. *J. Mater. Res. Technol.* **2023**, *27*, 5177–5190. [[CrossRef](#)]
78. Serdar, M.; Meral, C.; Kunz, M.; Dubravka, B.; Wenk, H.; Paulo, J. Spatial distribution of crystalline corrosion products formed during corrosion of stainless steel in concrete. *Cem. Concr. Res.* **2015**, *71*, 93–105. [[CrossRef](#)]

**Disclaimer/Publisher’s Note:** The statements, opinions and data contained in all publications are solely those of the individual author(s) and contributor(s) and not of MDPI and/or the editor(s). MDPI and/or the editor(s) disclaim responsibility for any injury to people or property resulting from any ideas, methods, instructions or products referred to in the content.